Surface structure determination by exhaustive search of asymmetric unit

Xingxing Dong,[1] Changchun He,[2] Chao He,[1] Hui Wang,[1] Shaogang Xu,[3] and Hu Xu[1,3,*]

[1]*Department of Physics, Southern University of Science and Technology, Shenzhen 518055, China*

[2]*Department of Physics, South China University of Technology, Guangzhou 510641, China*

[3]*Quantum Science Center of Guangdong-Hong Kong-Macao Greater Bay Area (Guangdong), Shenzhen 518045, China*

(Received 22 January 2024; revised 4 March 2024; accepted 14 March 2024; published 25 March 2024)

Determining surface structures is a substantial challenge due to the limitations of experimental techniques and the complexity of theoretical models. In this work, we use a method called the exhaustive search of asymmetric unit (ESAU), designed to identify surface structures through a detailed analysis of the asymmetric unit. This method employs two main strategies: narrowing the research area by focusing on a smaller, unique segment rather than the entire unit cell, and transforming the infinite possibilities of atomic positions into discrete, manageable units. These strategies allow us to systematically enumerate all potential surface structures. Employing the ESAU method, we have successfully replicated a variety of known surface structures, including two-dimensional materials on substrates, and have also uncovered some previously unknown structures. Importantly, the ESAU method shows significant promise not only in utilizing experimental data but also in predicting surface and crystal structures without prior experimental evidence. Our results affirm that the ESAU approach provides a comprehensive and efficient tool for uncovering material structures, paving the way for more in-depth studies on the properties and behaviors of materials.

DOI: 10.1103/PhysRevB.109.115430

I. INTRODUCTION

Surface research remains a vital field in materials science and condensed matter physics due to its significant impact on material behaviors and properties [1,2]. Understanding the atomic configurations of surfaces is essential for microscopic insights into material performance [3]. For instance, the structures of catalyst surfaces and their catalytic sites critically influence their efficiency, selectivity, and stability [4,5]. Additionally, knowledge of surface structures at various coverages is crucial for understanding growth mechanisms, which is essential for preparing high-quality samples through bottom-up approaches [6–8].

Nonetheless, determining surface structures remains a challenging task that typically involves comparing experimental data with simulations from hypothesized structural models. The traditional approach of manually building these models is heavily dependent on expert knowledge and susceptible to errors. For numerous surface systems, such as Si(111)-p(7×7) [9–12], Au(111)-p(5×5)-P [13–16], Pt(111)-p($4\sqrt{3}\times4\sqrt{3}$)R30°-P [17,18], Al(111)-p(3×3)-Ge [19–21], and Au(111)-Si [22–24], many models have been proposed before confirming their structures. Identifying surface structures demands selecting the most stable configuration within their phase space, a task challenging regardless of a researcher's expertise due to the continuous nature of atomic positions, the vast number of potential structures, and the extensive computational resources required. Algorithms such as random structure search [25], genetic algorithms, [26,27] and particle swarm optimization [28,29] have been developed to identify the most stable configurations. While these methods have pushed the field forward, they do not always guarantee finding the absolute ground state structures, mainly because they sample only a small portion of the phase spaces. Recent advancements in machine learning (ML) provide promising ways to reduce the significant computational effort needed to evaluate structural energies [30,31], opening up possibilities for more comprehensive exploration of the phase space.

In this study, we utilize the exhaustive search of asymmetric units (ESAU), a method designed for thorough structural enumeration. It focuses on minimal asymmetric regions and discrete atomic positioning, significantly cutting down computation time by substituting intensive density functional theory (DFT) calculations with an ML potential. The ESAU method has successfully reconstructed known surface structures and identified others. It also shows promise in predicting the structures of two-dimensional (2D) and three-dimensional (3D) materials without relying on prior experimental data. The ESAU method offers an automated and efficient approach for determining material structures, making it a valuable tool for the development of materials with superior properties.

II. COMPUTATIONAL METHODOLOGY

A. Training of on-the-fly machine learning force field (MLFF)

The MLFF is constructed using various structure datasets that define the Bravais lattice, atomic positions, total energies, forces, and stress tensors, all calculated by first-principles simulations [32–34]. For each structure, local configurations around each atom are identified with descriptors such as the radial and angular distributions of neighboring atoms [35],

*xuh@sustech.edu.cn

utilizing a cutoff radius of 5 Å to describe the local environment around each atom, and a 0.5 Å width for Gaussian functions to smooth atomic distributions. The MLFF is then fitted to these datasets and their local configurations, estimating the potential energy of a structure with N_a atoms by summing the local atomic potential energies [36],

$$U^{MLFF} = \sum_{i=1}^{N_a} U_i = \sum_{i=1}^{N_a} \sum_{i_b}^{N_b} w_{i_b} K(X_i, X_{i_b}),$$

where the linear combination of weight factors w_{i_b} and kernel functions $K(X_i, X_{i_b})$ represents each U_i. The kernel function assesses the similarity between local configurations around atom i and the reference local configuration i_b.

A Bayesian linear regression algorithm is utilized for on-the-fly ML, facilitating the prediction of total energies and forces [33]. This algorithm uses *ab initio* molecular dynamics (AIMD) simulations of varied structural configurations for learning. These configurations typically include a mix of isolated atoms, elemental and alloy clusters, and periodic monolayer structures (see Fig. S1) [37], ensuring a wide coverage of surface atom variations. For systems in this work, they were dynamically trained during AIMD simulations in the NVT ensemble, keeping the temperature and pressure through a Nose-Hoover thermostat [38]. During these MD calculations, *ab initio* data generated by the Vienna *ab initio* simulation package (VASP) [39,40] is collected and iteratively used to refine the training dataset for the ML model. Our strategy includes adding structures to the training set when the force error threshold is exceeded, with each new structure contributing new local configurations. Once the MLFF is obtained, at every time step, a Bayesian error threshold decides whether to perform an *ab initio* calculation and integrate the data into the force field or rely on MLFF predictions and forego further learning. As the force field accuracy improves, less sampling is required, allowing the model to skip more costly *ab initio* steps. Upon achieving a sufficiently precise force field, it can predict various properties efficiently. The algorithm for generating the on-the-fly force field and its effectiveness as an active learning strategy are documented in [33,41,42].

All first-principles calculations were carried out using DFT, as implemented in VASP [39,40]. We used the generalized gradient approximation with the Perdew-Burke-Ernzerhof scheme for exchange-correlation energy [43]. We set an energy cutoff of 450 eV for the plane-wave basis set, with a force convergence criterion of 0.02 eV/Å. We sampled the Brillouin zone with a uniform k-point mesh spacing of about 0.03 Å. For slab models, we included three substrate layers in the slab, with a vacuum space of 12 Å to avoid interactions between adjacent images. The bottom two substrate layers were fixed to mimic bulk conditions. No polarization effects were found in our studied systems, so dipole correction was omitted, as detailed in Sec. B of the Supplemental Material [37].

B. Generation of potential structures

The ESAU method aims to systematically identify the most stable structure by generating and evaluating all potential configurations within set symmetry parameters. It comprises two main stages: generation and evaluation, as illustrated in Fig. 1. The following subsections detail the ESAU method using the Au(111)-p(5×5)-P system as an example.

The crystal structure is defined by its lattice and the arrangement of atoms. The generation stage has four steps to enumerate all possible atomic combinations, depicted in Figs. 1(a)–1(e).

Step 1: Identify asymmetric regions by examining surface structure symmetry.

In crystallography, an asymmetric region is the smallest part of a crystal structure that can replicate the entire lattice through symmetry operations. These regions are often triangular or parallelogram shaped in 2D, as detailed in Sec. C of the Supplemental Material [37]. Techniques such as scanning tunneling microscopy (STM), atomic force microscopy (AFM), and low-energy electron diffraction (LEED) help identify these regions, offering insights into surface periodicity and symmetry. For instance, an STM image of Au(111)-P in Fig. 1(a) reveals a reconstructed unit cell lattice approximately 14.7 Å, suggesting a (5×5) supercell structure with *P6mm* symmetry [44]. The corresponding asymmetric region is a right-angled triangle, as shown in Fig. 1(b).

Step 2: Exhaustively generate asymmetric units.

Asymmetric units are generated by populating the identified asymmetric region with atoms or molecules, which together represent the full crystal structure. This process includes enumerating all possible asymmetric units by placing potential atomic or molecular sites within the asymmetric region. The set of all possible atom types, denoted as Atom $= \{\text{atom}_1, \text{atom}_2, \ldots, \text{atom}_m\}$, can be assigned to these sites, labeled as Site $= \{\text{site}_1, \text{site}_2, \ldots, \text{site}_n\}$. It is noteworthy that not every site needs to be occupied, allowing for some sites to remain vacant. Given atomic radii and the need for local optimization, adjacent sites are set approximately 2 Å apart. For the Au(111)-P system, the site set with nine evenly spaced sites (the gray spheres) within the asymmetric region and Atom $= \{\text{Au, P}\}$ is shown in Fig. 1(c). All possible arrangements are formulated by adding a P or Au atom or leaving a vacancy at each site, resulting in 3^9 (19 683) unique asymmetric units and surface configurations for the Au(111)-P system.

Step 3: Derive surface configurations from asymmetric units using symmetry operations.

Surface configurations for Au(111)-P, shown in Fig. 1(d), are obtained by applying the symmetry operations of the *P6mm* plane group to each asymmetric unit derived in step 2. This approach systematically creates diverse surface configurations that reflect the underlying symmetry of the crystal structure.

Step 4: Integrate surface configurations with the substrate to form complete surface slab models.

The final step involves integrating the various surface configurations with a substrate to produce complete surface slab models. As shown in Fig. 1(e), a standard slab model includes three parts: a vacuum region, a reconstruction region (the surface configuration), and a substrate region. This integration ensures that the resulting models are representative of actual surface structures, facilitating further analysis and evaluation.

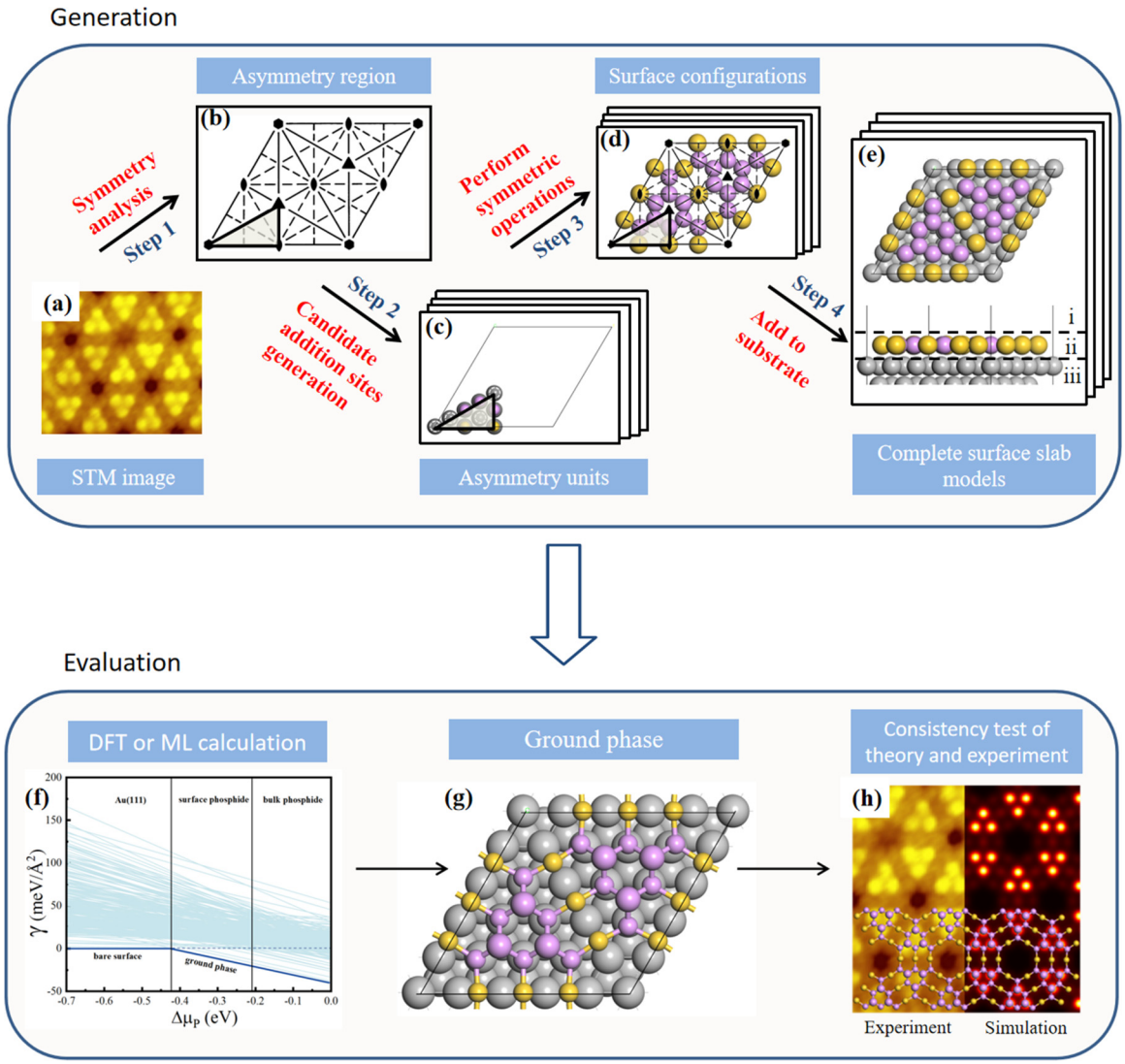

FIG. 1. Flowchart of the ESAU method, comprising two phases: generation and evaluation. Pink and yellow spheres represent P atoms and surface Au atoms, respectively, while gray spheres denote the Au(111) substrate. The experimental STM image is reproduced with permission from Ref. [44]. Copyright 2020 American Chemical Society.

C. Evaluation of structural stability

Phase diagrams are essential for depicting the stability of surface phases in relation to the chemical potential, serving as crucial predictive tools for understanding material behaviors under diverse conditions. The stability of surface structures, derived from the generation phase, is assessed using the following formula [45,46]:

$$\gamma = \frac{E_{\text{total}} - E_{\text{sub}} - N_{\text{s}} \times \mu_s - N_{\text{d}} \times \mu_{\text{d}}}{A},$$

where E_{total} and E_{sub} are the total energy of the system and the energy of the clean substrate, respectively. N_{s} and N_{d} are the numbers of substrate and deposited atoms in the surface configuration, respectively, and μ_{s} and μ_{d} are their chemical potentials. Notably, μ_{s} is the energy per atom in the bulk phase, and A denotes the surface area of the computational cell.

The ESAU method creates a wide range of potential surface structures and allows for cost-effective stability checks using ML potential. This strategy also enables efficient parallel processing. To speed up stability checks for about 20 000 Au(111)-P surface structures, this study uses MLFF techniques. Accurate interatomic potentials between Au and P atoms are derived using the on-the-fly ML model [47,48]. The training dataset includes around 1000 structures from AIMD simulations and has a root-mean-square error (RMSE) of 1.14 meV/atom, as shown in Fig. S2(a) [37]. To verify the reliability of MLFF, its energy predictions are compared with DFT results for a test set of 500 structures outside the training set. The standard deviation of the total energy across all structures in the training and test datasets is 26.91 eV and 11.56 eV, respectively, reflecting the broad range and diversity of our data. As shown in Fig. S2(a), the RMSE of energy for the test set is estimated as 1.25 meV/atom, much better than previous models for metal phosphides (9.50 meV/atom) [49].

The surface phase diagram of Au(111)-P, constructed using the ESAU method, highlights the most energetically favorable structures, as shown in Fig. 1(f). It identifies two main

structures that form the surface energy convex hull, marked by a blue line. For $\Delta\mu_P \leqslant -0.42$ eV, the Au(111) structure is preferred, while phosphorus-rich conditions ($\Delta\mu_P \geqslant -0.21$ eV) lead to surface phosphides, forming an Au-P network. As shown in Fig. 1(g), this network consists of two triangular blue phosphorene islands with nine P atoms each, connected by three Au atoms. Finally, to align simulations with experimental results, the study confirms the most stable structure through simulated STM image, matching well with experimental data, as shown in Fig. 1(h). These findings agree well with previous studies on phosphorus deposition onto Au(111) surfaces [16]. Additionally, Table S2 summarizes the computational resources required to evaluate the numerous phases generated by ESAU across different systems [37], offering insights into the computational demands and efficiencies of our approach.

III. RESULTS AND DISCUSSION

A. Surface oxides on Ag(111)

In addition to the Au(111)-P system, the Ag(111)-O system is another example of how well the ESAU method works. This system is extensively studied due to the widespread use of silver catalysts in industrial processes, particularly for converting methanol into various chemicals and for synthesizing epoxides from propylene [50,51]. High oxygen coverage is known to prompt the formation of the c(4×8) phase [52,53], identifiable through the matrix $\begin{pmatrix} 3 & 1 \\ 1 & 3 \end{pmatrix}$. Despite previous studies identifying this structure, they often required significant computational resources [54,55]. By using the ESAU method, we have made finding this surface phase more efficient.

Generation. The STM image in Fig. 2(a) shows the pattern of the Ag(111)-O surface, which is about 7.76 Å across and has a *P4mm* symmetry [52,53]. Its asymmetric region is a right-angled triangle that takes up 1/8 of the total area, as you can see in Fig. S4 [37]. So, we focus on a smaller right triangle with sides of 3.88 Å and a hypotenuse of 5.49 Å, as shown in Fig. 2(a). In this region, we identify eight possible spots for atoms, called Site = {site $_1$, site$_2$, …, site$_8$}. We then mix and match these spots with O or Ag atoms or leave them empty to create 3^8 (6561) different asymmetric units. Through symmetrical operations of the *P4mm* planar group, various surface configurations are created and combined with a clean substrate to model the surface accurately.

Evaluation. Because the Ag(111)-O surface cell is quite small, we could use DFT calculations for all the models to create a surface energy phase diagram that shows how the stability changes with the chemical potential of oxygen, as seen in Fig. 2(b). This diagram has three important parts: (i) The clean Ag surface is stable for $\Delta\mu_O \leqslant -0.56$ eV. (ii) Surface oxides form between $-0.56\,\text{eV} \leqslant \Delta\mu_O \leqslant -0.31$ eV. (iii) When $\Delta\mu_O \geqslant -0.31$ eV, the surface oxides turn into the bulk phase, forming Ag_2O. Notably, only one stable surface phase emerges throughout this oxidation process.

Figure 2(c) shows the atomic arrangement of this stable phase, which has a repeating pattern of Ag_4O_4 units (marked in yellow) linking Ag atoms. This phase, labeled Ag_5O_4,

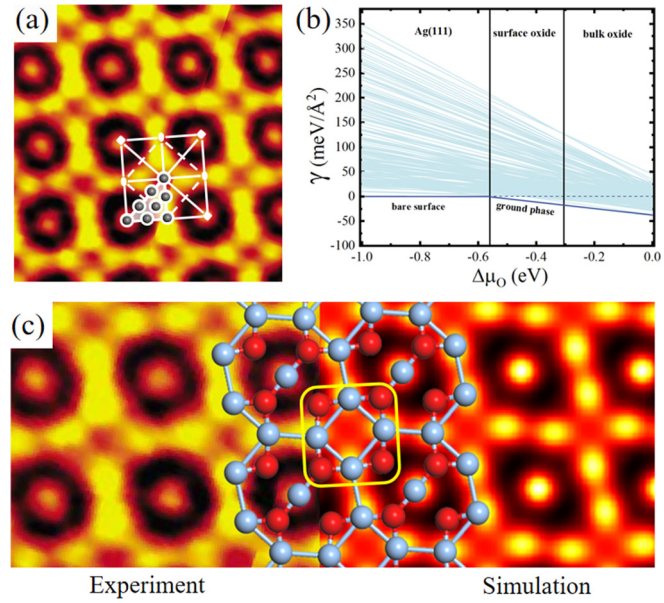

FIG. 2. Establishing the structure of the Ag(111)-$\begin{pmatrix} 3 & 1 \\ 1 & 3 \end{pmatrix}$-O surface. (a) STM image of the Ag(111)-$\begin{pmatrix} 3 & 1 \\ 1 & 3 \end{pmatrix}$-O, alongside a distribution diagram of symmetric elements in the *P4mm* space group. (b) Surface phase diagram depicting the oxidation of the Ag(111) surface as a function of oxygen chemical potential. (c) Preferred atomic configuration superimposed on the experimental image (left) compared with the simulated image (right). The spheres in red and blue represent O atoms and surface Ag atoms, respectively. The experimental STM image is reproduced with permission [52]. Copyright 2009 American Physical Society.

exhibits O and Ag coverages of 0.50 and 0.62 atomic layers (AL), respectively, consistent with the known c(4×8) structure on Ag(111) [52,53]. Furthermore, the simulated STM images match very well with the actual experimental observations, as shown in Fig. 2(c). These findings confirm the ability of ESAU to accurately identify the most stable phase on the oxidized Ag surface.

B. Antimony deposited on Pt(111)

The success of graphene has sparked intensive research into 2D materials [56–58]. Beyond exfoliation, scientists are particularly interested in synthesizing 2D materials on substrates [6–8]. However, recent studies have raised questions about the feasibility of forming pure layers of these materials on metal substrates [16,18,21,24], and some surface structures also remain unclear at the atomic level. We use the ESAU method to investigate the complex Pt(111)-Sb surface structure.

Generation. After depositing Sb onto the Pt(111) substrate, a p($5\sqrt{3}\times5\sqrt{3}$)R30° pattern emerges, distinct from the underlying metal lattice [59]. The STM image in Fig. 3(a) reveals clear protrusions, suggesting a *P6mm* symmetry. The reconstructed unit cell, spanning approximately 24.30 Å, features an asymmetric region forming a right triangle, occupying 1/12 of the cell, as highlighted in Fig. 3(b). To thoroughly explore potential surface configurations, we identify 20 sites for Sb, Pt atoms, or vacancies, leading to a staggering 3^{20}

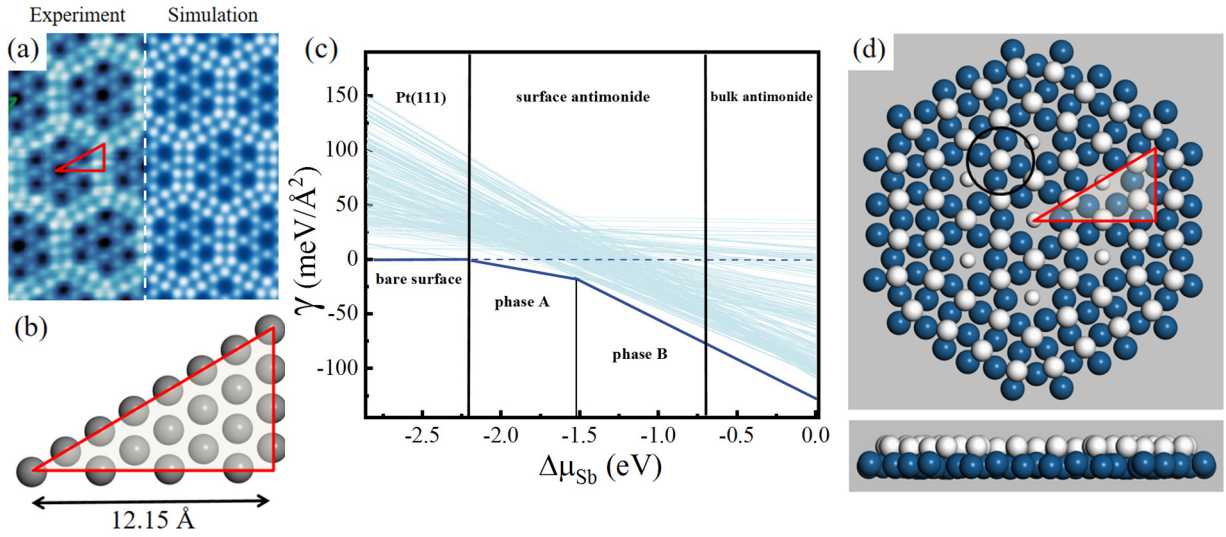

FIG. 3. Determination of the Pt(111)-p($5\sqrt{3}\times5\sqrt{3}$)R30°-Sb surface structure. (a) Experimental and simulated STM images of the Pt(111)-p($5\sqrt{3}\times5\sqrt{3}$)R30°-Sb structure. (b) The asymmetric region and potential addition sites on Pt(111)-p($5\sqrt{3}\times5\sqrt{3}$)R30°-Sb. (c) Surface phase diagram for Pt(111)-Sb as a function of antimony chemical potential. (d) Most stable atomic configuration of the Pt(111)-Sb surface under Sb-rich conditions. The white and dark green spheres denote Sb and surface Pt atoms, respectively. The experimental STM image is reproduced with permission [59].

unique configurations. By focusing on the most symmetrical configurations, we reduce the asymmetric region, narrowing down the potential sites to 9 (3^9), detailed in Sec. D of the Supplemental Material [37]. These 3^9 asymmetric units are transformed through symmetry operations to generate various surface models.

Evaluation. With over 225 atoms in the superstructure, it is costly to optimize each model using conventional methods. Therefore, we employ the MLFF method to decrease computational costs and accelerate the optimization process. The ML potential, trained on approximately 1000 structures, show good agreement between the training and test data, as visually confirmed in Fig. S2(b) [37]. For the Pt(111)-Sb system, the total energy standard deviation for all structures in the training and test datasets is 36.25 eV and 25.24 eV, respectively. The calculated RMSEs for the energy of the training and test sets are 1.02 and 4.37 meV/atom, respectively, suggesting that the ML potential performs well in energy prediction and its feasibility as an alternative to DFT.

We construct a surface energy phase diagram to assess the models, showing the chemical potential energy variation with Sb, as shown in Fig. 3(c). The diagram identifies three distinct regions based on $\Delta\mu_{\mathrm{Sb}}$. For $\Delta\mu_{\mathrm{Sb}} \leqslant -2.20$ eV, the clean Pt(111) surface remains stable. From -2.20 eV $\leqslant \Delta\mu_{\mathrm{Sb}} \leqslant -0.71$ eV, surface antimonides emerge. Above $\Delta\mu_{\mathrm{Sb}} \geqslant -0.71$ eV, the Pt substrate undergoes a phase transition into Sb_2Pt. Within the surface alloys, two distinct structures constitute the surface energy convex hull. For -2.20 eV $\leqslant \Delta\mu_{\mathrm{Sb}} \leqslant -1.53$ eV, 12 Sb atoms occupy hollow sites, creating phase A, detailed in Fig. S6(a) [37]. In Sb-rich conditions ($\Delta\mu_{\mathrm{Sb}} \geqslant -1.53$ eV), phase B forms a continuous surface alloy layer, composed of $Pt_{60}Sb_{37}$, as seen in Figs. 3(d) and S6(b). This phase features edge-sharing Pt_4Sb motifs with Sb atoms on the substrate. Each Pt_4Sb motif, highlighted in Fig. 3(d), presents four Pt atoms in a square, with an Sb atom at Pt_4-hollow sites, resembling structures found with VA group elements like P on Pt(111) [18]. Additionally, an Sb atom sits at the center of a ring formed by six Pt_4Sb motifs.

The experimental data and simulations of the $Pt_{60}Sb_{37}$ model align closely, predicting an Sb atom coverage of 0.49 AL, which closely matches the experimental measurement of 0.5 AL [59]. The simulated STM image, depicted in Fig. 3(a), corresponding well with experimental observations, features 30 unit cell protrusions indicative of Sb atoms in Pt_4Sb motifs. To verify the thermal stability of the $Pt_{60}Sb_{37}$ model, MD simulations were conducted at 700 K, just above the experimental annealing temperature of 380 °C [59]. As shown in Fig. S7 [37], the $Pt_{60}Sb_{37}$ model maintains its structure without significant changes after 50 ps, affirming its energetic and thermodynamic stability.

C. Unveiling 3D structures and predicting potential structures

The ESAU method is not just for surfaces and it also helps us understand freestanding 2D materials and 3D bulk materials. For freestanding 2D materials, we bypass the final step in the generation phase to directly examine the stability of surface configurations. For 3D materials, we incorporate an additional dimension to identify potential sites within the asymmetric region, a step crucial for 3D regions. For instance, the asymmetric region for the space groups $P6_3/mmc$ (No. 194) and $P4/mmm$ (No. 99) is both a triangular prism, as shown in Figs. 4(a) and 4(b).

We apply the ESAU method to investigate the structures of the Na-Bi binary alloy. The stable compounds found in the Na-Bi system through experiments are Na_3Bi ($P6_3/mmc$) and

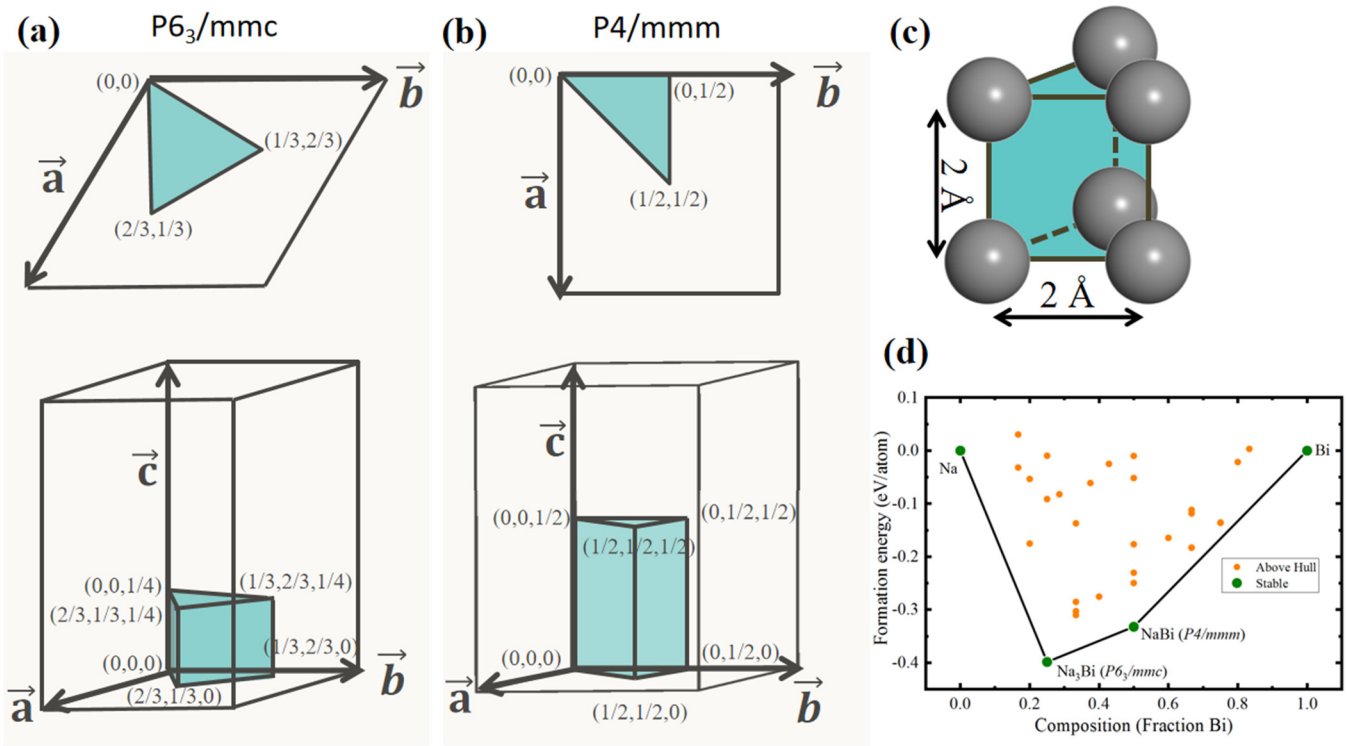

FIG. 4. Structure identification of the Na-Bi alloy with the $P6_3/mmc$ and P4/mmm space group. The asymmetric region within the (a) $P6_3/mmc$ and (b) P4/mmm space group. (c) An asymmetric region of 2 Å in both length and height. (c) The convex hull diagram of Na-Bi alloys.

NaBi ($P4/mmm$), as reported in previous studies [49,60]. As shown in Figs. 4(a) and 4(b), the asymmetric regions of these space groups form regular and right-angled triangular prisms, covering 1/24 and 1/16 of the unit cell volume, respectively. We start with a simple asymmetric region with six potential sites at the apex, as depicted in Fig. 4(c). By introducing a Na atom, a Bi atom, or a vacancy at each site, we generate 3^6 (729) crystal structures for each space group.

To evaluate the stability of these alloys, we construct a convex hull diagram using calculated formation energies as follows: $E_{\text{form}} = (E_{\text{total}} - N_{\text{Na}} \times E_{\text{Na}} - N_{\text{Bi}} \times E_{\text{Bi}})/(N_{\text{Na}} + N_{\text{Bi}})$, where E_{total}, E_{Na}, and E_{Bi} are the energies of the entire system, single Na atom, and single Bi atom in their respective bulks. N_{Na} and N_{Bi} represent the numbers of Na atoms and Bi atoms in the alloy, respectively. Structures on the convex hull are thermodynamically stable, as shown in Fig. 4(c), with two structures (Na_3Bi and NaBi) identified and detailed in Fig. S8 [37]. Notably, NaBi is recognized as a bulk superconductor [61], and Na_3Bi is of interest as a 3D topological Dirac semimetal, promising for potential applications [62–64]. Our ESAU method has confirmed two thermodynamically stable structures, in excellent agreement with previous experimental reports [49,60].

The ESAU method, based on experimental data like lattice parameters and symmetry, is effective in identifying the ground state phase. It also holds promise for predicting new structures without prior experimental data. To thoroughly explore a new system, we need to generate all possible structures with various lattices, prioritizing those with higher symmetry since they are more likely to be lower in energy. For unexplored lattices, we start with smaller asymmetric regions, expanding gradually. While exploring new structures without experimental references increases computational requirements, advancements in computational methods and resources are anticipated to facilitate the prediction of new structures across a wide range of materials.

IV. CONCLUSION

In this work, we introduce the ESAU method for identifying surface structures. This method characterized by its focus on the detailed examination of asymmetric regions and the discretization of atomic positions, facilitates a comprehensive exploration of potential surface configurations. Additionally, we employ reliable ML potentials to speed up the stability analysis. The versatility of the ESAU method makes it incredibly useful for surface science research. Its generation and evaluation steps are flexible and can be adapted to various systems. As shown through examples in this work, the ESAU method is not only good at replicating already known structures but also excellent at unveiling others, thereby expanding our understanding of material surfaces. It represents a significant improvement over traditional, intuition-based manual methods, offering a deeper insight into the microscopic properties of materials.

ACKNOWLEDGMENT

This work is supported by the National Natural Science Foundation of China (Grant No. 12374182),

the Shenzhen Science and Technology Program (Grant No. RCYX20200714114523069), and the Center for Computational Science and Engineering at Southern University of Science and Technology.

[1] U. Diebold, The surface science of titanium dioxide, Surf. Sci. Rep. **48**, 53 (2003).
[2] R. M. Hewlett and M. A. McLachlan, Surface structure modification of ZnO and the impact on electronic properties, Adv. Mater. **28**, 3893 (2016).
[3] J. Kibsgaard, Z. Chen, B. N. Reinecke, and T. F. Jaramillo, Engineering the surface structure of MoS_2 to preferentially expose active edge sites for electrocatalysis, Nat. Mater. **11**, 963 (2012).
[4] Z.-Y. Zhou, N. Tian, J.-T. Li, I. Broadwell, and S.-G. Sun, Nanomaterials of high surface energy with exceptional properties in catalysis and energy storage, Chem. Soc. Rev. **40**, 4167 (2011).
[5] H. Tian, Y. He, Q. Zhao, J. Li, X. Shao, Z. Zhang, X. Huang, C. Lu, K. Wang, Q. Jiang, A. Ng, H. Xu, and S. Tong, Avoiding Sabatier's conflict in bifunctional heterogeneous catalysts for the WGS reaction, Chem **7**, 1271 (2021).
[6] F.-F. Zhu, W.-J. Chen, Y. Xu, C.-L. Gao, D.-D. Guan, C.-H. Liu, D. Qian, S.-C. Zhang, and J.-F. Jia, Epitaxial growth of two-dimensional stanene, Nat. Mater. **14**, 1020 (2015).
[7] E. Salomon, R. El Ajjouri, G. Le Lay, and T. Angot, Growth and structural properties of silicene at multilayer coverage, J. Phys.: Condens. Matter **26**, 185003 (2014).
[8] L. Huang, Y.-F. Zhang, Y.-Y. Zhang, W. Xu, Y. Que, E. Li, J.-B. Pan, Y.-L. Wang, Y. Liu, S.-X. Du *et al.*, Sequence of silicon monolayer structures grown on a Ru surface: From a herringbone structure to silicene, Nano Lett. **17**, 1161 (2017).
[9] K. Takayanagi, Y. Tanishiro, S. Takahashi, and M. Takahashi, Structure analysis of Si(111)-7×7 reconstructed surface by transmission electron diffraction, Surf. Sci. **164**, 367 (1985).
[10] K. Takayanagi and Y. Tanishiro, Dimer-chain model for the 7×7 and the 2×8 reconstructed surfaces of reconstructed surfaces of Si(111) and Ge(111), Phys. Rev. B **34**, 1034 (1986).
[11] G. Binnig, H. Rohrer, C. Gerber, and E. Weibel, 7×7 Reconstruction on Si(111) Resolved in Real Space, Phys. Rev. Lett. **50**, 120 (1983).
[12] K. D. Brommer, M. Needels, B. E. Larson, and J. D. Joannopoulos, *Ab initio* theory of the Si(111)-(7×7) surface reconstruction: A challenge for massively parallel computation, Phys. Rev. Lett. **68**, 1355 (1992).
[13] J. L. Zhang, S. Zhao, C. Han, Z. Wang, S. Zhong, S. Sun, R. Guo, X. Zhou, C. D. Gu, K. D. Yuan, Z. Li, and W. Chen, Epitaxial growth of single layer blue phosphorus: A new phase of two-dimensional phosphorus, Nano Lett. **16**, 4903 (2016).
[14] J. Zhuang, C. Liu, Q. Gao, Y. Liu, H. Feng, X. Xu, J. Wang, J. Zhao, S. X. Dou, Z. Hu, and Y. Du, Band gap modulated by electronic superlattice in blue phosphorene, ACS Nano **12**, 5059 (2018).
[15] W. Zhang, H. Enriquez, Y. Tong, A. Bendounan, A. Kara, A. P. Seitsonen, A. J. Mayne, G. Dujardin, and H. Oughaddou, Epitaxial synthesis of blue phosphorene, Small **14**, 1804066 (2018).
[16] H. Tian, J.-Q. Zhang, W. Ho, J.-P. Xu, B. Xia, Y. Xia, J. Fan, H. Xu, M. Xie, and S. Tong, Two-dimensional metal-phosphorus network, Matter **2**, 111 (2020).
[17] O. Heikkinen, H. Pinto, G. Sinha, S. K. Hämäläinen, J. Sainio, S. Öberg, P. R. Briddon, A. S. Foster, and J. Lahtinen, Characterization of a hexagonal phosphorus adlayer on platinum (111), J. Phys. Chem. C **119**, 12291 (2015).
[18] J. Zhang, X. Dong, S. Xu, Y. Xia, W. Ho, H. Xu, and M. Xie, Metal-phosphorus network on Pt (111), 2D Mater. **9**, 045002 (2022).
[19] E. A. Martínez, J. D. Fuhr, O. Grizzi, E. A. Sánchez, and E. D. Cantero, Growth of germanene on al(111) hindered by surface alloy formation, J. Phys. Chem. C **123**, 12910 (2019).
[20] K. Zhang, D. Sciacca, M.-C. Hanf, R. Bernard, Y. Borensztein, A. Resta, Y. Garreau, A. Vlad, A. Coati, I. Lefebvre, M. Derivaz, C. Pirri, P. Sonnet, R. Stephan, and G. Prévot, Structure of germanene/al(111): A two-layer surface alloy, J. Phys. Chem. C **125**, 24702 (2021).
[21] F. Yan, S. Xu, C. He, C. He, C. Zhao, and H. Xu, Identifying the alloy structures of germanene grown on Al(111), Phys. Rev. B **106**, 075405 (2022).
[22] S. Sadeddine, H. Enriquez, A. Bendounan, P. Kumar Das, I. Vobornik, A. Kara, A. J. Mayne, F. Sirotti, G. Dujardin, and H. Oughaddou, Compelling experimental evidence of a Dirac cone in the electronic structure of a 2D Silicon layer, Sci. Rep. **7**, 44400 (2017).
[23] A. Stpniak-Dybala, P. Dyniec, M. Kopciuszyski, R. Zdyb, M. Jałochowski, and M. Krawiec, Planar silicene: a new silicon allotrope epitaxially grown by segregation, Adv. Funct. Mater. **29**, 1906053 (2019).
[24] C.-C. He, S.-G. Xu, S.-B. Qiu, C. He, Y.-J. Zhao, X.-B. Yang, and H. Xu, Five-fold symmetry in Au-Si metallic glass, Nanoscale **14**, 12757 (2022).
[25] C. J. Pickard and R. Needs, *Ab initio* random structure searching, J. Phys.: Condens. Matter **23**, 053201 (2011).
[26] S. Wu, M. Ji, C.-Z. Wang, M. C. Nguyen, X. Zhao, K. Umemoto, R. Wentzcovitch, and K.-M. Ho, An adaptive genetic algorithm for crystal structure prediction, J. Phys.: Condens. Matter **26**, 035402 (2014).
[27] C. W. Glass, A. R. Oganov, and N. Hansen, USPEX'Evolutionary crystal structure prediction, Comput. Phys. Commun. **175**, 713 (2006).
[28] F. Marini and B. Walczak, Particle swarm optimization (PSO). A tutorial, Chemometr. Intell. Lab. **149**, 153 (2015).
[29] Y. Wang, J. Lv, L. Zhu, and Y. Ma, CALYPSO: A method for crystal structure prediction, Comput. Phys. Commun. **183**, 2063 (2012).
[30] R. Gómez-Bombarelli, J. Aguilera-Iparraguirre, T. D. Hirzel, D. Duvenaud, D. Maclaurin, M. A. Blood-Forsythe, H. S. Chae, M. Einzinger, D.-G. Ha, T. Wu *et al.*, Design of efficient molecular organic light-emitting diodes by a high-throughput virtual screening and experimental approach, Nat. Mater. **15**, 1120 (2016).
[31] Y. Yang, O. A. Jiménez-Negrón, and J. R. Kitchin, Machine-learning accelerated geometry optimization in molecular simulation, J. Chem. Phys. **154**, 234704 (2021).

[32] R. Jinnouchi, J. Lahnsteiner, F. Karsai, G. Kresse, and M. Bokdam, Phase transitions of hybrid perovskites simulated by machine-learning force fields trained on the fly with bayesian inference, Phys. Rev. Lett. **122**, 225701 (2019).

[33] R. Jinnouchi, F. Karsai, and G. Kresse, On-the-fly machine learning force field generation: Application to melting points, Phys. Rev. B **100**, 014105 (2019).

[34] R. Jinnouchi, F. Karsai, C. Verdi, R. Asahi, and G. Kresse, Descriptors representing two- and three-body atomic distributions and their effects on the accuracy of machine-learned inter-atomic potentials, J. Chem. Phys. **152**, 234102, 234102 (2020).

[35] A. P. Bartók, R. Kondor, and G. Csányi, On representing chemical environments, Phys. Rev. B **87**, 184115 (2013).

[36] J. Behler and M. Parrinello, Generalized neural-network representation of high-dimensional potential-energy surfaces, Phys. Rev. Lett. **98**, 146401 (2007).

[37] See Supplemental Material http://link.aps.org/supplemental/10.1103/PhysRevB.109.115430 for the detailed information about the on-the-fly MLFF training, dipole correction test, asymmetric regions for all planar groups, detailed information about the Pt(111)-Sb and Na-Bi systems, and the computational efforts for each system.

[38] S. Nosé, A unified formulation of the constant temperature molecular dynamics methods, J. Chem. Phys. **81**, 511 (1984).

[39] G. Kresse and J. Furthmüller, Efficiency of *ab-initio* total energy calculations for metals and semiconductors using a plane-wave basis set, Comput. Mater. Sci. **6**, 15 (1996).

[40] G. Kresse and J. Furthmüller, Efficient iterative schemes for *ab initio* total-energy calculations using a plane-wave basis set, Phys. Rev. B **54**, 11169 (1996).

[41] E. V. Podryabinkin and A. V. Shapeev, Active learning of linearly parametrized interatomic potentials, Comput. Mater. Sci. **140**, 171 (2017).

[42] C. Cui, Y. Zhang, T. Ouyang, M. Chen, C. Tang, Q. Chen, C. He, J. Li, and J. Zhong, On-the-fly machine learning potential accelerated accurate prediction of lattice thermal conductivity of metastable silicon crystals, Phys. Rev. Mater. **7**, 033803 (2023).

[43] J. P. Perdew, K. Burke, and M. Ernzerhof, Generalized gradient approximation made simple, Phys. Rev. Lett. **77**, 3865 (1996).

[44] J. L. Zhang, S. Zhao, S. Sun, H. Ding, J. Hu, Y. Li, Q. Xu, X. Yu, M. Telychko, J. Su *et al.*, Synthesis of monolayer blue phosphorus enabled by silicon intercalation, ACS Nano **14**, 3687 (2020).

[45] A. Michaelides, M.-L. Bocquet, P. Sautet, A. Alavi, and D. King, Structures and thermodynamic phase transitions for oxygen and silver oxide phases on Ag(111), Chem. Phys. Lett. **367**, 344 (2003).

[46] R. B. Wexler, T. Qiu, and A. M. Rappe, Automatic prediction of surface phase diagrams using *ab initio* grand canonical Monte Carlo, J. Phys. Chem. C **123**, 2321 (2019).

[47] M. A. Caro, Optimizing many-body atomic descriptors for enhanced computational performance of machine learning based interatomic potentials, Phys. Rev. B **100**, 024112 (2019).

[48] D. Ormoneit and Ś. Sen, Kernel-based reinforcement learning, Mach. Learn. **49**, 161 (2002).

[49] C. Zhang, Y. Sun, H.-D. Wang, F. Zhang, T.-Q. Wen, K.-M. Ho, and C.-Z. Wang, Crystallization of the P_3Sn_4 phase upon cooling P_2Sn_5 liquid by molecular dynamics simulation using a machine learning interatomic potential, J. Phys. Chem. C **125**, 3127 (2021).

[50] S. J. Khatib and S. Oyama, Direct oxidation of propylene to propylene oxide with molecular oxygen: a review, Catal. Rev. **57**, 306 (2015).

[51] T. A. Nijhuis, M. Makkee, J. A. Moulijn, and B. M. Weckhuysen, The production of propene oxide: catalytic processes and recent developments, Ind. Eng. Chem. Res. **45**, 3447 (2006).

[52] J. Schnadt, J. Knudsen, X. L. Hu, A. Michaelides, R. T. Vang, K. Reuter, Z. Li, E. Lægsgaard, M. Scheffler, and F. Besenbacher, Experimental and theoretical study of oxygen adsorption structures on Ag(111), Phys. Rev. B **80**, 075424 (2009).

[53] N. Martin, S. Klacar, H. Gronbeck, J. Knudsen, J. Schnadt, S. Blomberg, J. Gustafson, and E. Lundgren, High-coverage oxygen-induced surface structures on Ag (111), J. Phys. Chem. C **118**, 15324 (2014).

[54] D. Chen, C. Shang, and Z.-P. Liu, Automated search for optimal surface phases (ASOPs) in grand canonical ensemble powered by machine learning, J. Chem. Phys. **156**, 094104 (2022).

[55] N. Rønne, M.-P. V. Christiansen, A. M. Slavensky, Z. Tang, F. Brix, M. E. Pedersen, M. K. Bisbo, and B. Hammer, Atomistic structure search using local surrogate model, J. Chem. Phys. **157**, 174115 (2022).

[56] K. S. Novoselov, A. K. Geim, S. V. Morozov, D. Jiang, Y. Zhang, S. V. Dubonos, I. V. Grigorieva, and A. A. Firsov, Electric field effect in atomically thin carbon films, Science **306**, 666 (2004).

[57] R. Mas-Balleste, C. Gomez-Navarro, J. Gomez-Herrero, and F. Zamora, 2D materials: to graphene and beyond, Nanoscale **3**, 20 (2011).

[58] A. Gupta, T. Sakthivel, and S. Seal, Recent development in 2D materials beyond graphene, Prog. Mater. Sci. **73**, 44 (2015).

[59] H. Guo, M. D. Jiménez-Sánchez, A. J. Martínez-Galera, and J. M. Gómez-Rodríguez, Unraveling the highly complex nature of antimony on Pt (111), Adv. Mater. Interfaces **9**, 2101272 (2022).

[60] J. Sangster and A. D. Pelton, The Bi-Na (Bismuth-Sodium) system, J. Phase Equilib. **12**, 451 (1991).

[61] S. K. Kushwaha, J. W. Krizan, J. Xiong, T. Klimczuk, Q. D. Gibson, T. Liang, N. P. Ong, and R. J. Cava, Superconducting properties and electronic structure of NaBi, J. Phys.: Condens. Matter **26**, 212201 (2014).

[62] Z. K. Liu, B. Zhou, Y. Zhang, Z. J. Wang, H. M. Weng, D. Prabhakaran, S.-K. Mo, Z. X. Shen, Z. Fang, X. Dai, Z. Hussain, and Y. L. Chen, Discovery of a Three-Dimensional Topological Dirac Semimetal, Na_3Bi, Science **343**, 864 (2014).

[63] J. Xiong, S. K. Kushwaha, T. Liang, J. W. Krizan, M. Hirschberger, W. Wang, R. J. Cava, and N. P. Ong, Evidence for the chiral anomaly in the Dirac semimetal Na_3Bi, Science **350**, 413 (2015).

[64] S. Liang, J. Lin, S. Kushwaha, J. Xing, N. Ni, R. J. Cava, and N. P. Ong, Experimental tests of the chiral anomaly magnetoresistance in the dirac-weyl semimetals Na_3Bi and GdPtBi, Phys. Rev. X **8**, 031002 (2018).